Research article

Multiomics profiling uncovers curdione-induced reproductive toxicity in HTR-8/SVneo cells

Qibin Wu [a,1], Mengting Chen [b,1], Yifan Lin [b,1], Jian Zhang [b], Xinyue Gao [b], Yajiao Wu [b], Caijin Wu [a], Jiaxin Wen [b], Jiaqi Li [b], Chutao Li [b], Wenqiang Bao [b], Dongcheng Zhang [b], Meijin Zheng [a,*], An Zhu [a,b,**]

[a] Fujian Maternity and Child Health Hospital, College of Clinical Medicine for Obstetrics & Gynecology and Pediatrics, Fujian Medical University, Fuzhou 350001, China
[b] Key Laboratory of Gastrointestinal Cancer (Fujian Medical University), Ministry of Education, Fuzhou, 350108, China

ARTICLE INFO

ABSTRACT

The assessment of medication toxicity and safety is pivotal during pregnancy. Curdione, a sesquiterpene compound extracted from *Curcumae Radix*, displays beneficial properties in terms of anti-inflammatory, tumor growth suppression, and anti-coagulative effects. However, its reproductive toxicity and precise mechanism remain unclear. This study aims to explore the mechanism of curdione-induced toxicity damage in HTR-8/SVneo cells through the epigenetics, proteomics, and metabolomics, and experimental verification. The results showed that curdione elicited alterations in m6A modification, gene expression, protein levels, and cellular metabolism of HTR-8/SVneo cells. Additionally, curdione induces oxidative stress, mitochondrial and DNA damage, while also downregulating the expression of Wnt6, β-catenin, ZO-1, and CLDN1 proteins. Curdione has the potential to modulate oxidative stress, mitochondrial dysfunction, and disruption of tight junctions via the Wnt/β-catenin signaling pathway, which contributes to cellular damage in HTR-8/SVneo cells.

1. Introduction

Curdione, derived from *Curcumae Radix*, is a sesquiterpenoid known for its diverse pharmacological properties, including inhibiting platelet aggregation, reducing inflammation, combating tumors, and protecting against neurodegenerative conditions [1,2]. The perspective that traditional Chinese medicine can produce adverse effects in addition to having medicinal properties has been presented. Research studies have reported that the administration of 15.5 mg/kg of white peony root and 10 mg/kg of raw rehmannia root to pregnant mice can affect fetal development, resulting in stillbirth, postnatal death, delayed birth, or congenital abnormalities [3]. Additionally, it has been found that pregnant SD rats exposed to curdione from gestational day 6 to gestational day 15 faced a potential risk of accumulation, which might affect the fetus by crossing the placental barrier system [4]. Studies have shown that numerous
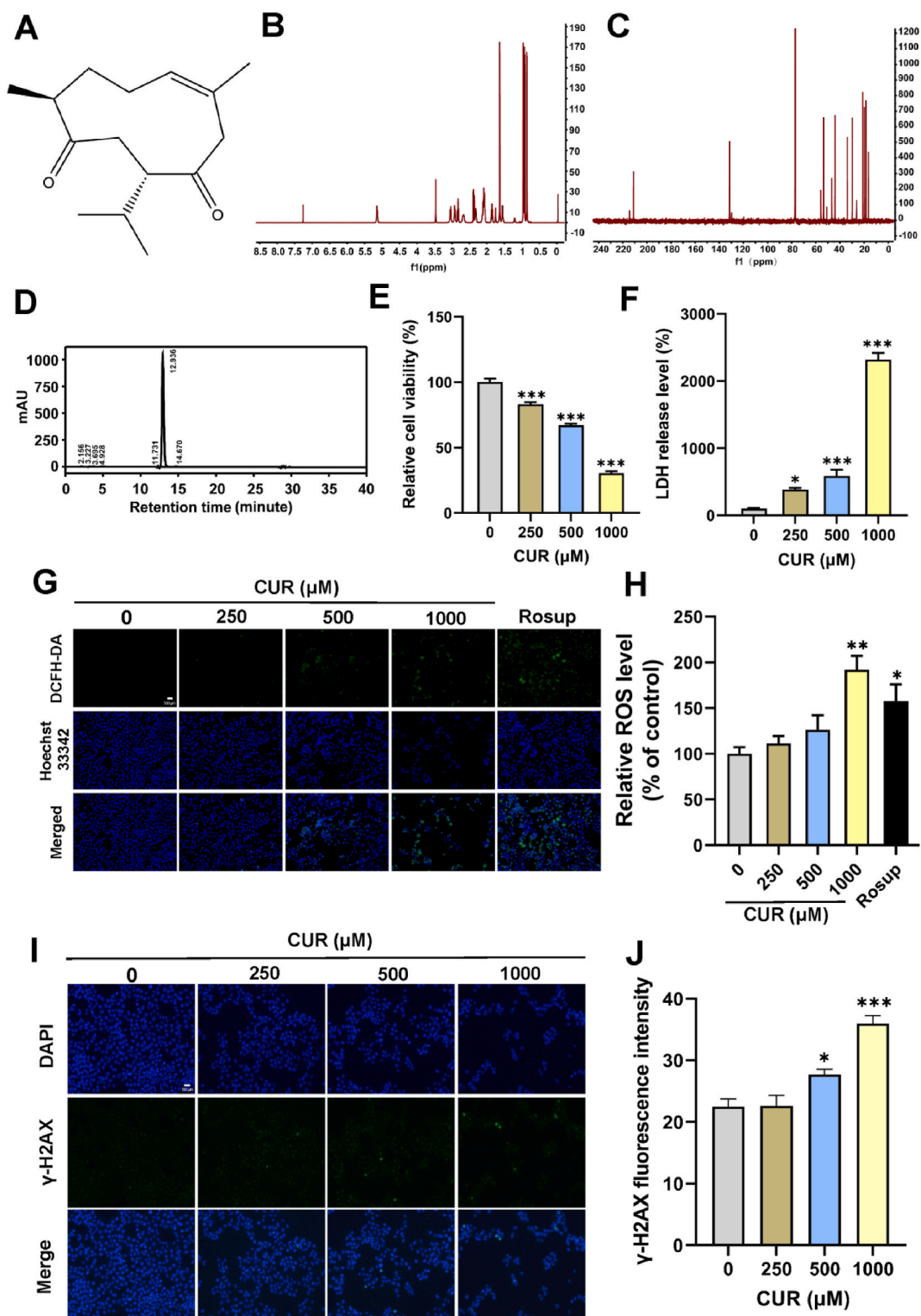
Fig. 1. (A) The chemical structure of curdione. (B) 400 MHz ^{1}H NMR spectra of curdione. (C) 400 MHz ^{13}C NMR spectra of curdione. (D) Analysis of curdione purity using HPLC. Cytotoxicity of curdione to HTR-8/SVneo cells. The concentration effect of curdione on (E) cell viability and (F) LDH release level. The cell viability and LDH release level in the treated groups were expressed as percentages. Effects of curdione exposure on the intracellular ROS production in HTR-8/SVneo cells. (G) Representative images showing the intracellular ROS production. (H) Analysis of the relative fluorescence levels of DCF in both the control and treated groups. (I) The levels of phosphorylated γ-H2AX induced by curdione were analyzed using a fluorescent microscope. (J) Quantitative results of γ-H2AX fluorescence. $*p < 0.05$, $**p < 0.01$ or $***p < 0.001$.

components of traditional Chinese medicine possess reproductive toxicity, but there are few reports on the reproductive toxicity of curdione. Given that it is a component of traditional Chinese medicine, it is postulated that curdione might possess reproductive toxicity, and this study aims to explore its possible toxic mechanisms.

Over the past few decades, omics techniques have been demonstrated to be a potent instrument for investigating the interactions between drugs and biomolecules. By employing computer modeling and bioinformatics, omics can offer comprehensive insights into the mechanisms behind biological processes and functions, such as potential targets and critical pathways [5]. The recent advancements in sequencing techniques have demonstrated that RNA methylation is a prevalent and functionally significant modification implicated in the regulation of gene expression [6,7]. N6-methyladenosine (m6A) represents the predominant mRNA modification identified within mammal, and is essential for modulating gene expression [8]. The m6A protein regulators interact with mRNA molecules to read, catalyze, or remove methylation modifications based on cellular requirements, having a critical function in governing diverse cellular and biological processes [9–11]. Alterations in m6A modification have been linked to abnormal reproductive development. Increased levels of mRNA m6A content in ALKBH5-deficient male mice have been associated with impaired fertility due to mid-meiosis spermatocyte apoptosis [12]. Moreover, the effects of numerous traditional Chinese medicine components on the cell state are attributed to their interference with the mechanisms of transcription and translation. A study has shown that curdione induces ferroptosis in CT26 cells and SW480 cells through m6A methylation, namely by upregulating the expression of YTHDF2 and METTL14 [13]. On the other hand, toxic metabolomics seeks to identify toxicity-related biomarkers by analyzing characteristic alterations in endogenous metabolite levels in biological fluids, aiding in toxicity assessment and understanding toxicological processes [14]. While transcriptomics, epigenomics, and proteomics can reveal the roles of toxicants directly or indirectly, metabolites act as the end products of specific biological processes, reflecting reactions that have already taken place [5]. Combining multiomics approaches can enhance the discovery of drug targets and potential modes of action, playing a vital role in comprehending drug reactions from a systemic perspective.

Cellular metabolism relies heavily on mitochondria, which function as a central modulator of redox stability. When mitochondria suffer damage or dysfunction, their capacity to produce energy is compromised and significant amounts of reactive oxygen species (ROS) are generated. Concurrently, mitochondria are susceptible to damage inflicted by ROS. A study revealed that the rise in impaired mitochondrial membrane potential occurred in a dose-dependent way following treatment with diverse concentrations of curdione in Michigan Cancer Foundation-7 cells for 72 h [15].

In embryonic development, organogenesis, tissue regeneration, and a range of physiological processes, the Wnt family member (Wnt) signaling pathway serves as a central player. Moreover, the dysregulation of this pathway is intricately linked to diverse pathological conditions. The Wnt signaling pathway has a dual function, both in the stabilizing of β-catenin and regulating gene expression inside the nucleus, as well as in the maintenance of the cytoskeleton outside the nucleus [16]. The involvement of Wnt in the control of cell–cell communication has been validated through the interplay of β-catenin and E-cadherin, which is crucial for maintaining cell adhesion. However, the mechanism by which the Wnt signaling pathway regulates mitochondrial damage and tight junction in curdione-induced reproductive toxicity is still unclear.

The HTR-8/SVneo cell is an immortalized human placental chorionic cell line that was isolated from the placenta of a 6-to-12-week-old embryo. In this study, high-throughput m6A MeRIP-seq, transcriptomics, proteomics, and metabonomics were utilized to investigate the mechanism of reproductive toxicity caused by curdione in the HTR-8/SVneo cell line. Curdione was found to trigger mitochondrial damage and disrupt tight junctions, possibly through mediation by the Wnt signaling pathway.

2. Materials and methods

2.1. Cultivation of curdione in HTR-8/SVneo cells

The chemical constructure of curdione is presented in Fig. 1A. Curdione was sourced from Must Bio-Technology Co., Ltd. (Chengdu, China), and exhibited a concentration of 98.92 %. The purity was validated using high-performance liquid chromatography (HPLC) (Fig. 1D), along with 400 MHz ^{1}H and ^{13}C nuclear magnetic resonance spectroscopy illustrated in Fig. 1B and C, respectively. Human extravillous trophoblast cell line, HTR-8/SVneo cells were cultured in Dulbecco's modified Eagle's medium (DMEM) with 10 % fetal bovine serum in a maintenance environment with a temperature 37 °C and 5 % CO_2. By dissolving curdione in dimethyl sulfoxide (DMSO) and subsequently performing dilutions in DMEM, solutions with concentrations of 250, 500, and 1000 μM were obtained, which were applied to HTR-8/SVneo cells once they reached 80 % confluence. The designated final concentration for cell culture was 1 % DMSO.

2.2. Cell viability and lactate dehydrogenase (LDH) leakage assay

To determine HTR-8/SVneo cell viability, the cells were seeded into 96-well plates. After that, the cells were subjected to curdione treatment at 250, 500, and 1000 μM concentrations. Following exposure of the cells to curdione and upon reaching the predetermined time of 48 h, 120 μL of cell supernatant was taken from each well and subsequently incubated with LDH detection reagent for 30 min to assess LDH leakage. The LDH detection reagent consisted of lactate solution, 2-p-iodophenyl-3-nitrophenyltetrazolium chloride solution (1 ×), and enzyme solution. Subsequently, the MTT solution was introduced and the mixture was incubated for 4 h at 37 °C. Each well was analyzed for optical density at 490 nm by means of a microplate reader manufactured by BioTek (Santa Clara, CA, USA) [17].

2.3. RNA extraction

HTR-8/SVneo cells were placed into 6 cm dishes with curdione at 500 μM for 48 h, followed by PBS washing. Trizol reagent (Invitrogen, Carlsbad, CA, USA) was used for the total RNA extraction, followed by dissolution in RNAse-free water. The assessment of RNA concentration and quality involved the examination of the A260/A280 ratio. The eligible RNA underwent final quantification using Qubit3.0 (Thermo Fishe, Waltham, MA, USA) for high-throughput sequence.

2.4. High-throughput m6A MeRIP-seq and mRNA-seq

Seqhealth (Wuhan, China) applied high-throughput MeRIP-seq to study the m6A methylation changes in RNAs. The process began with 50 μg of total RNAs for the enrichment of polyadenylated RNA, using VAHTS mRNA Capture Beads (Vazyme Biotech, Nanjing, China). Following this, m6A immunoprecipitation (IP) was conducted using a particular anti-m6A antibody (Synaptic Systems, Goettingen, Lower Saxony, Germany) and a 100–200 nt mRNA fragment produced through the treatment of mRNA with 20 mM $ZnCl_2$ at 95 °C for 10 min. Part of the mRNA fragment was saved as 'Input' in reserve. Subsequently, library products ranging from 200 to 500 base pairs in size were enriched and sequenced on a Novaseq 6000 sequencer (Illumina).

The differentially expressed genes (DEGs) between the curdione teratment group and the control group were screened by *p* value and fold change. All the assembled clusters were entered into exomePeak2 [18], Homer [19], Hisat2 [20], DEseq2 [21], RMDisease2 [22], consRM [23], MetaTX [24], and DAVID [25] to obtain RIP-Seq peak predictions, motifs analysis, and enrichment.

2.5. Molecular docking

The crystal model of the m6A regulators were acquired from the Protein Data Bank (PDB) and homology modeling. The structure of curdione was downloaded from PubChem as a mol2 format file, followed by structural energy minimization and semi-flexibility docking using SYBYL-X 2.0. In this study, a total score of more than 5 points is considered indicative of stable binding between the ligand and protein [26].

2.6. Sample preparation and proteomics analysis

2.6.1. Sample extraction and peptide digestion

Upon exposure to 500 μM of curdione for 48 h, the HTR-8/SVneo cells were lysed, and the resulting lysate was subjected to centrifugation (Centrifuge 5840R) at 12,000 ×*g* for 10 min at 4 °C to obtain the supernatant. Quantification of the protein extraction from each sample resulted in 150 μg, which was then subjected to reduction using 200 mM Tris (2-carboxyethyl) phosphine hydrochloride for 1h and alkylation with 375 mM iodoacetamide for 30 min. Then six times the volume of acetone to the sample was included and left to incubate for 4 h at −20 °C. The precipitate was collected after a brief centrifugation of 5 min at 1000 ×*g* and subsequently air-dried. The above products were then mixed with a 200 mM triethylammonium bicarbonate buffer and subjected to overnight incubation at 37 °C in the presence of trypsin.

2.6.2. Tandem mass tag fractionation and LC-MS/MS analysis

The peptides were split into 15 fractions and dehydrated afterwards using vacuum centrifugation. For LC-MS/MS analysis, the pre-fractionated peptides were dissolved in 0.1 % formic acid and introduced into an 25 cm × 75 μm Acclaim PepMap C18 column (Thermo Fisher). The Orbitrap Exploris 480 MS was then applied to analyze the separated peptides. With a resolution of 60,000 FWHM, MS1 spectra covering a mass range from 350 to 1600 *m/z* were acquired using an AGC target set at 300 %. Fragmentation of the top 12 precursor ions was performed using higher-energy collisional dissociation in data-dependent mode. At a resolution of 30,000 and with TurboTMT enabled, the MS/MS scan was conducted.

2.6.3. Performing database search on MS data

The data output was processed using Proteome Discoverer 3.0, and it was matched against *Homo sapiens* Uniprot database (20,605 sequences, downloaded in May 2023). Carbamidomethyl for cysteine, TMTpro (Cat#A44520, Thermo Fisher) for lysine and the N-terminus were applied as fixed modifications, while methionine oxidation and protein N-terminus acetylation were set as variable modifications. Two missed cleavages were allowed, the length of variable post-translational modifications per peptide ranged from 3 to 7.

2.7. Metabolomics sample preparation and analysis

For a duration of 48 h, 500 μM curdione was used to treat HTR-8/SVneo cells, and then immersed in liquid nitrogen for 10 min after being washed with PBS, which were prepared for UPLC-MS/MS analysis conducted by Metware (Wuhan, China). 300 μL extraction solution containing internal standards and 20 % acetonitrile was added to the cells and vortexed for 3 min. The supernatant was collected via centrifugation at 12,000 ×*g*, and was repeated after a 30 min incubation.

ACQUITY UPLC HSS T3 C18 column (1.8 μm, 2.1 mm × 100 mm) from Waters (Milford, MA, USA) was used to inject the samples. The solvent system consisted of water with 0.1 % formic acid (mobile phase A) and acetonitrile with 0.1 % formic acid (mobile phase B). The gradient profile of the mobile phase is detailed below: mobile phase B followed by a linear gradient from 5 % to 90 % over 11

min, held for 1 min, and then returned to 5 % within 0.1 min and maintained for 1.9 min. Raw data on metabolism from the mass spectrometry was loaded into MetaboScape 2022 (Bruker, Karlsruhe, Baden-Wurttemberg, Germany) for accuracy assessment. Then quantitative information of metabolites was matched from NIST Chemistry WebBook, Human Metabolome Database, personnel and public databases. Following screening and adjustments, the data was prepared for subsequent bioinformatics and functional analyses.

2.8. The cytotoxicity of curdione

2.8.1. Intracellular ROS accumulation

The fluorescent probe 2′,7′-dichlorofluorescein diacetate (DCFH-DA) (Solarbio, Beijing, China) was utilized to quantify ROS levels. Following a 48 h exposure to 0, 250, 500, and 1000 μM curdione, cells were cultured with 10 μM DCFH-DA at a temperature of 37 °C in darkness for 30 min. Visualization and analysis were conducted using a Zeiss fluorescent microscope (Oberkochen, Germany) and ImageJ.

2.8.2. Immunofluorescence staining of γ-H2AX

The measurement of γ-H2AX immunofluorescence staining was conducted using the DNA damage assay kit (Beyotime, Shanghai, China). After a 48 h incubation with curdione at doses of 0, 250, 500, and 1000 μM, the cells were treated with QuickBlock Blocking Buffer (Beyotime) for 15 min. The next step involved incubating the cells with a γ-H2AX primary antibody at room temperature for 1 h. The HTR-8/SVneo cells were washed and incubated with a488-labeled anti-rabbit secondary antibody. Following three washes, 4′,6-diamidino-2-phenylindole (DAPI) was used to stain the nuclei, and samples were subsequently imaged using a fluorescence microscope (Zeiss).

2.8.3. Cellular calcium detection

After 48 h of 0, 250, 500, and 1000 μM curdione exposure, Fluo-4 AM (Beyotime) was employed as an intracellular Ca^{2+} indicator to measure the Ca^{2+} concentrations in HTR-8/SVneo cells. The cells were treated with PBS wash followed by incubation at 37 °C for 1 h with 1 μM Fluo-4 AM solution in PBS. The intracellular Ca^{2+} concentration changes were investigated using a fluorescence microscope (Zeiss) with excitation at 494 nm and emission at 516 nm.

2.8.4. Measurement of mitochondrial membrane potential

The JC-10 probe from Solarbio was used to evaluate the mitochondrial membrane potential (MMP). Typically, the MMP maintains a relatively high state. Aggregates are formed by the JC-10 probe within the mitochondria, leading to the emission of red fluorescence. In the case of mitochondrial damage, the membrane potential declines, preventing the aggregation of JC-10 in the matrix. In this situation, JC-10 exists as monomers and emits green fluorescence. The decrease in MMP can be easily identified when red fluorescence shifts to green.

After 48 h of 0, 250, 500, and 1000 μM curdione exposure, the HTR-8/SVneo cells underwent a 20 min incubation with the JC-10 probe following manual. Subsequently, a Zeiss microscope was employed to analyze the red and green fluorescence.

2.8.5. Detection of mitochondrial permeability transition pore (mPTP)

The curdione-exposed cells were treated at 37 °C with the Calcein AM probe for 40 min. Following this, the probe was removed and the nucleus was subjected to staining with hoechst 33342 for a duration of 15 min. The green fluorescence was examined under a microscope (Zeiss) after being washed by PBS.

Table 1
Primers for RT-qPCR used in this study.

Gene	Primer sequence (5'→3')
GSK3B	GCACTCTTCAACTTCACCACTCAAG (F)
	CTGTCCACGGTCTCCAGTATTAGC (R)
C-MYC	GTCTGGATCACCTTCTGCTGGAG (F)
	GCTGCGTAGTTGTGCTGATGTG (R)
β-catenin	ATAGAGGCTCTTGTGCGTACTGTC (F)
	TTGGTGTCGGCTGGTCAGATG (R)
WNT6	CTCCTCTACGCCGCCGATTC (F)
	GCCGCAGCACAGCAGGTC (R)
TCF7L1	GGAGCCGAGCAGCGATAGC (F)
	CCTCTCCGCCTCCGAGTCC (R)
CLDN1	TGGTGGTTGGCATCCTCCTG (F)
	TCATCGTCTTCCAAGCACTTCATAC (R)
TJP1	GCGGATGGTGCTACAAGTGATG (F)
	GCCTTCTGTGTCTGTGTCTTCATAG (R)
OCLN	ACTTCGCCTGTGGATGACTTCAG (F)
	TTCTCTTTGACCTTCCTGCTCTTCC (R)
GAPDH	TGACATCAAGAAGGTGGTGAAGCAG (F)
	GTGTCGCTGTTGAAGTCAGAGGAG (R)

2.9. RT-qPCR

Following 48-h treatment with 0, 250, 500, and 1000 μM curdione. RNA extraction was performed as described previously. The concentration was quantified to 1000 ng in RNAse-free water and reverse transcribed into cDNA using reverse transcription premixed kit (Accurate Biology, Changsha, China). RT-qPCR was performed using the AtiaMX Real-Time PCR System from Agilent (Santa Clara, CA, USA). The $2^{-\Delta\Delta Ct}$ method [27] was then applied to calculate relative gene expression under curdione treatment. Primers used in this experiment can be found in Table 1. As an endogenous control for the other target genes, the expression of GAPDH was utilized.

2.10. Western blotting analysis

After treatment with 0, 250, 500 and 1000 μM curdione for 48 h, the HTR-8/SVneo cells were lysed by RIPA (Beyotime). The protein was collected following ultrasonication and a brief centrifugation at 12,000 ×g for 10 min at 4 °C, after which the supernatant was collected. Following separation via 12 % sodium dodecyl sulfate-polyacrylamide gel electrophoresis, the protein lysates were transferred onto polyvinylidene fluoride membranes (Millipore, Billerica, MA, USA). Following a 1.5 h blocking step using 5 % non-fat milk, the membranes were incubated with Wnt family member 6 (Wnt6) (1:1000, Proteintech, Wuhan, China), β-catenin (1:10,000, Proteintech), glycogen synthase kinase 3B (GSK3B) (1:4500, Proteintech), cyclin D1 (CCND1) (1:10,000, Proteintech), C-MYC
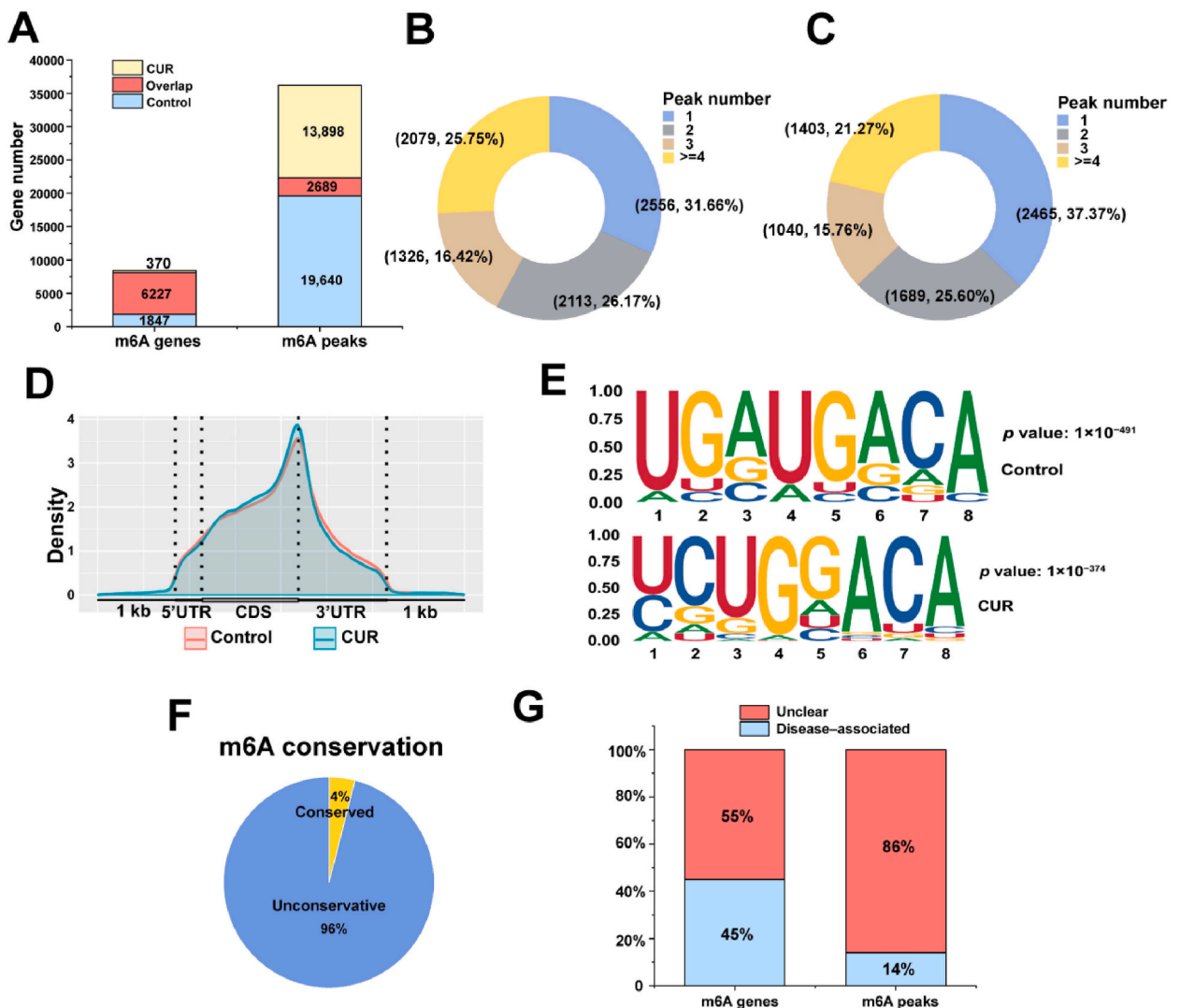

Fig. 2. (A) The bar chart illustrated the intersection of the m6A gene and m6A peaks between the control and curdione groups. The number of genes corresponding to the peak number of m6A was observed in both the control group (B) and the curdione group (C). The density (D) of m6A modification peaks identified for each genes. (E) The top enriched motifs within m6A peaks in two groups. (F) The conservation of m6A sites and (G) disease-associated m6A genes and m6A peaks.

(1:10,000, Proteintech), claudin-1 (CLDN1) (1:4500, Proteintech), transcription Factor 7 like 1 (TCF7L1) (1:1000, Proteintech) and zonula occludens-1 (ZO-1) (1:10,000, Proteintech) antibodies, as well as the internal control GAPDH (1:12,000, Proteintech) antibody overnight at 4 °C. Then, the membranes were incubated with corresponding secondary antibodies at room temperature for 1.5 h (1:10,000, Proteintech). The signals were detected with the ECL-chemiluminescent kit (HRbio, Fujian, China) [28] after washing in TBST buffer.
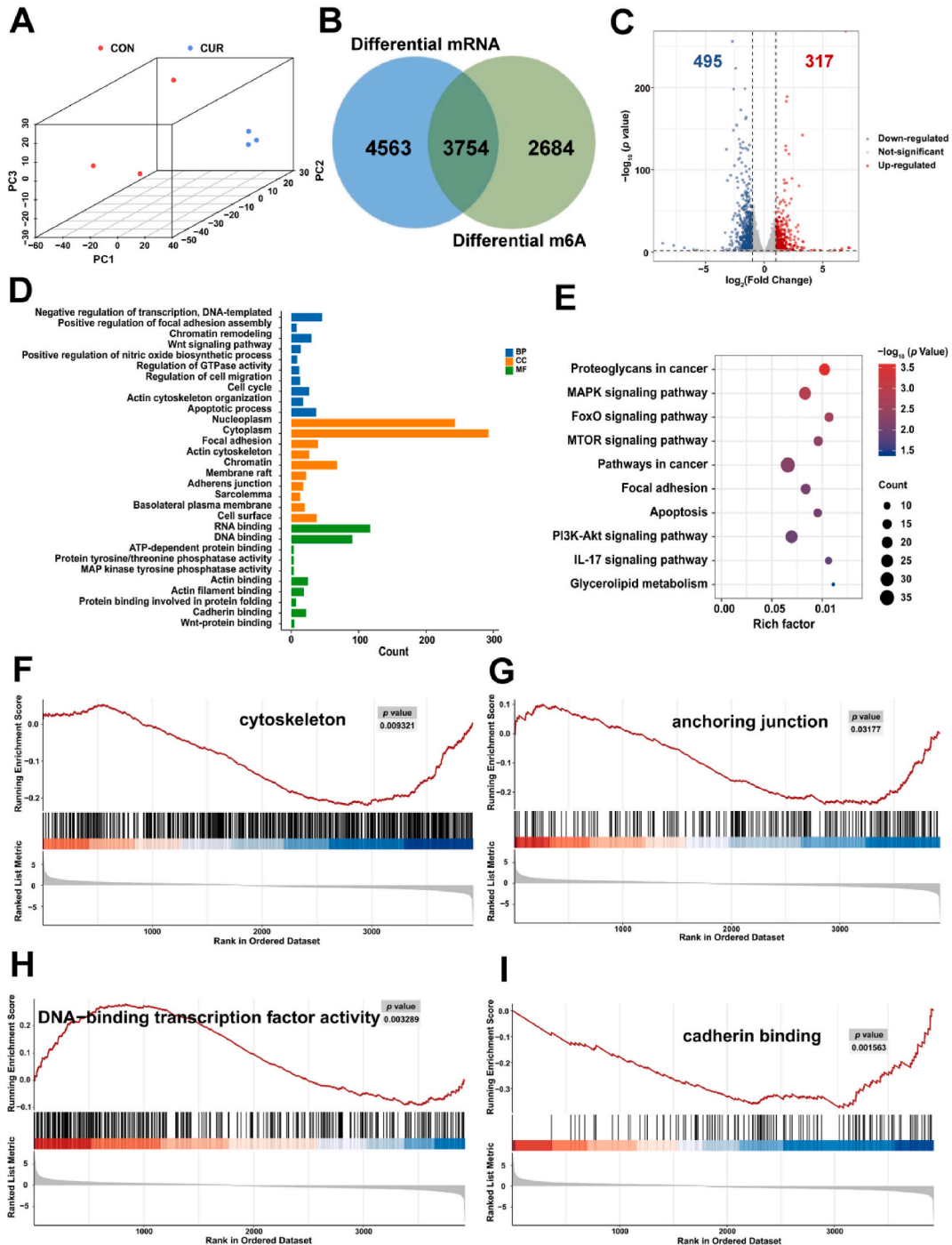

Fig. 3. (A) The PCA diagram of the control and curdione groups. (B) Venn plot showing the overlap of differentially m6A genes and mRNA. (C) Volcano plot of the 3997 overlapping genes. The GO (D) and KEGG (E) enrichment of significant differential genes. The GSEA analysis were enriched in cytoskeleton (F), anchoring junction (G), DNA-binding transcription factor activity (H), and cadherin binding (I).

2.11. Statistical analysis

Data analysis was conducted using SPSS 26 software (IBM, New York, NY, USA). The results are shown as the mean $\pm$ standard deviation (SEM). One-way ANOVA was used to compare group variances, with statistical significance determined at $p < 0.05$. Each experiment was repeated at least three independent trials.

3. Results

3.1. Effects of curdione on the cell viability and LDH release in HTR-8/SVneo cells

The viability of cells decreased significantly in correlation with curdione concentration. After 48 h of exposure to 250, 500, and 1000 μM curdione, the cell relative viability was found to be 83.2 %, 67.3 %, and 30.6 %, respectively (Fig. 1E). The LDH assay was employed to confirm the cytotoxicity of curdione. After 48 h of exposure to curdione concentrations of 250, 500, and 1000 μM, the levels of LDH release from the cells, the levels of LDH release exhibited a significant increase, reaching 3.8, 5.9, and 23.2 times above those of the control group, respectively (Fig. 1F).

3.2. Effects of curdione on the ROS and γ-H2AX accumulation in HTR-8/SVneo cells

In order to evaluate the cellular oxidative stress condition, the intracellular content of ROS was measured. The ROS fluorescence diagram illustrated that the intensity of the green spots correlated with the intracellular ROS level, and a higher fluorescence indicated an increased ROS production within the cells. As shown in Fig. 1G and H, the trend of luminosity revealed that the fluorescence intensity of all treated groups exceeded that of the control group significantly. The fluorescence quantitative values (Fig. 1I and J) of γ-H2AX were 22.5 ± 2.18, 22.66 ± 2.91, 27.72 ± 1.45, and 35.98 ± 6.03 in the 0, 250, 500, and 1000 μM curdione groups respectively, indicating a concentration-dependent increase. Curdione was found to cause oxidative stress and DNA damage according to the results.

3.3. Analysis of MeRIP-Seq data uncovers the m6A modification profile following curdione treatment

To clarify the changes in post-transcriptional modifications after treating the HTR-8/SVneo cells with curdione, MeRIP-seq was performed after treating the cells with 500 μM curdione for 48 h. Fig. 2A illustrated that a total of 8074 and 6597 m6A-modified genes, as well as 22,329 and 16,587 m6A peaks were found in the control and curdione groups, respectively. At the intersection of these two groups, 6227 genes with m6A modifications and 2689 m6A peaks were identified. In Fig. 2B and C, it can be observed that the majority of genes displayed between one and four m6A peaks, with more than 2000 genes exhibiting one peak. The distribution of m6A methylation showed that m6A peaks were highly enriched around the stop codon, and rapidly decreased in the 3′UTR region in the control and curdione groups (Fig. 2D). To identify the motif of m6A modification, both the control group and the curdione group were found to match the m6A consensus sequence of RRACH (Fig. 2E). The degree of conservation for individual m6A sites was assessed using ConsRM, revealing that 96 % of the m6A modified sites were unconservative (Fig. 2F). As shown in Fig. 2G, 45 % of genes

Table 2
The mRNA expression levels of m6A regulators in curdione-treated HTR-8/SVneo cells.

Gene	Regulation	Base Mean	log$_2$FoldChange	$p$adj
WTAP	writer	5677	0.8500	2.13×10^{-37}
YTHDF3	reader	1232	2.0577	2.02×10^{-26}
RBM15B	writer	2948	−1.3726	1.47×10^{-25}
HNRNPA2B1	reader	119,936	−0.7537	1.17×10^{-22}
HNRNPC	reader	59401	−0.7310	2.44×10^{-18}
YTHDF1	reader	3506	0.6775	3.80×10^{-14}
FTO	eraser	1792	0.7911	8.23×10^{-13}
CBLL1	writer	1858	0.7820	3.92×10^{-10}
IGF2BP3	reader	1529	−0.6243	5.25×10^{-8}
ZC3H13	writer	34,020	−0.4618	8.53×10^{-7}
METTL14	writer	5337	0.4092	2.73×10^{-6}
IGF2BP2	reader	11,016	−0.3303	8.36×10^{-5}
VIRMA	writer	7725	−0.4138	8.57×10^{-5}
YTHDC1	reader	14,781	−0.3872	2.88×10^{-2}
FMR1	reader	4184	0.2053	3.18×10^{-2}
METTL5	writer	2895	0.2391	3.73×10^{-2}
RBM15	writer	1462	1.2344	3.73×10^{-2}
YTHDF2	reader	1422	−0.2310	1.61×10^{-1}
ALKBH5	eraser	14,532	0.1618	1.75×10^{-1}
IGF2BP1	reader	7454	−0.3036	1.77×10^{-1}
YTHDC2	reader	1667	0.1169	4.35×10^{-1}
METTL3	writer	1630	−0.0198	9.06×10^{-1}

associated with m6A modifications and 14 % of m6A peaks are correlated with the disease.

3.4. Combined analysis of RNA-seq and mRNA-seq

The PCA plots indicated notable clustering differences between the control and treatment groups (Fig. 3A). By comparing the 6681 m6A gene set and the 8560 RNA-seq genes with $p < 0.05$ following the differential analysis, it was revealed that 3754 genes displayed significant differences between the two groups (Fig. 3B). The overlapping genes were screened based on a fold change >2 or <0.5, with a p value < 0.01, resulting in the identification of 317 up-regulated genes and 495 down-regulated genes (Fig. 3C). The GO enrichment analysis (Fig. 3D) revealed enrichment of the Wnt signaling pathway, focal adhesion, DNA binding, actin cytoskeleton, and cadherin binding. Moreover, various KEGG pathways analyses (Fig. 3E) showed significant enrichments in the focal adhesion pathways, apoptosis pathways, and glycerolipid metabolism pathway. The DEGs that meet the criteria of |log$_2$fold change| > 1 and have a p value < 0.01 of RNA-seq are shown in Table S1. The cytoskeleton, anchoring junction, and cadherin binding pathway were inhibited, while the DNA-binding transcription factor activity was activated based on the gene set enrichment analysis (GSEA) analyses (Fig. 3F–I).

3.5. Molecular docking between curdione and m6A regulatory proteins

Molecular docking was used in this study to simulate the interaction between curdione and the top ten m6A regulators listed in Table 2. The predicted results with a total score are shown in Table 3, while the docking model depicted in Fig. 4A–D exhibits a total docking score exceeding 5. Hydrogen bonds were detected between curdione and Arg96, and His231 within the fat mass and obesity-associated protein (FTO), alongside Arg86 and Lys150 in insulin like growth factor 2 mRNA binding protein 3 (IGF2BP3). FTO exhibited hydrophobic contacts with curdione at the Tyr108, Val228, Ser318, Arg316, Val309, Thr320, Tyr295, and Arg322 sites, whereas IGF2BP3 demonstrated hydrophobic interactions with curdione at the Ser58, Lys60, Val70, Glu71, and Ile54 sites.

To delve into the genes regulated by differentially expressed m6A regulators, the writer RNA-binding motif protein 15B (RBM15B) and RBM15, reader YTH N6-methyladenosine RNA binding protein F3 (YTHDF3), YTHDF1, YTHDC1, IGF2BP3, IGF2BP2, heterogeneous nuclear ribonucleoprotein C (HNRNPC), and fragile X mental retardation protein 1 (FMR1) were selected, as well as the genes related to the focal adhesion, Wnt signaling pathway, Wnt-protein binding, and cell cycle from GO and KEGG enrichment (Fig. 4E). According to the predictive results, HNRNPC was found to be implicated in the regulation of the aforementioned four processes. The analysis of m6A methylation levels on transcripts was conducted using Integrated Genomics Viewer (IGV), as shown in Fig. 4F.

3.6. Analysis of the effect of curdione on HTR-8/SVneo cells via proteomics

Analysis of the raw data through PCA was employed to investigate the effect of curdione treatment (500 μM, 48 h) on protein accumulation in the HTR-8/SVneo cells, as depicted in Fig. 5A. The results indicate the significant impact of curdione treatment on protein accumulation in HTR-8/SVneo cells. Volcano plot was used to demonstrate the DEPs chosen according to the criterion of a p

Table 3

The molecular interaction between curdione and m6A regulatory proteins through docking analysis.

| Protein	PDB or Uniprot ID	Reference	Total score	Crash	Polar	H- bond number	Residues involved in H-bond formation	Hydrophobic contact number	Residues involve in hydrophobic contacts
FTO	7E8Z	(Shishodia et al., 2021)	5.40	−3.73	2.4956	2	Arg96, His231	8	Tyr108, Val228, Ser318, Arg316, Val309, Thr320, Tyr295, Arg322
IGF2BP3	6FQ1	(Jia et al., 2018)	5.14	−0.87	2.4879	2	Arg86, Lys150	5	Ser58, Lys60, Val70, Glu71, Ile54
RBM15B	Q8NDT2	AlphaFold prediction	5.24	−0.43	0.668	1	Arg819	6	Tyr827, Leu728, Lys729, Ser731, Asn730, Gln817
WTAP	7YFJ	(Yan et al., 2022)	3.45	−0.53	1.038	1	Tyr64	3	Glu67, Leu68, Gln72
YTHDF3	8BS5	–	3.55	−0.88	1.926	2	Arg447 (2 H-bonds)	3	Thr535, His443, Lys446
HNRNPA2B1	5EN1	(Wu et al., 2018)	4.38	−0.69	1.017	1	Lys104	6	Arg185, Val97, Val170, Leu171, Glu101, Ala107
HNRNPC	2MXY	(Cienikováet al., 2014)	4.06	−0.43	1.625	2	Arg99 (2 H-bonds)	5	Gly96, Lys98, Val90, Asn91, Glu103
ZC3H13	7VF2	(Su et al., 2022)	6.22	−1.47	0	–	–	8	Glu1579, Lys1520, Arg1529, Leu1553, Ala1525, Leu1528, Leu1576, Leu1575
YTHDF1	8BS4	–	4.71	−1.15	0.0002	–	–	8	Glu546, Gln543, Arg542, Tyr539, Asp400, Lys469, Gln467, Arg404
CBLL1	Q75N03	AlphaFold prediction	3.94	−0.58	1.194	–	–	6	Gln170, Val197, Arg199, Pro196, Ile168, Thr198
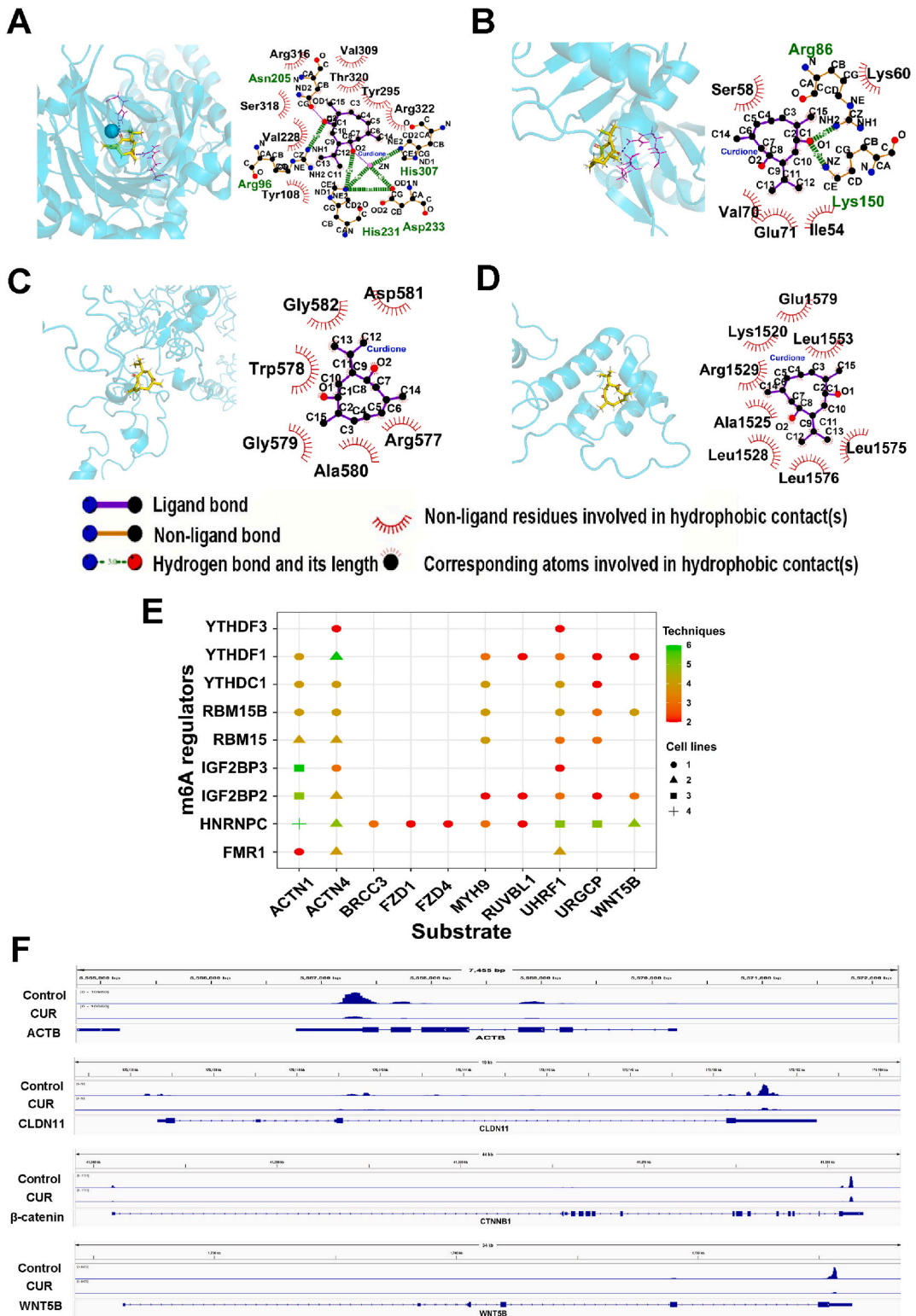
Fig. 4. The 2D and 3D molecular interaction models between curdione and m6A regulators of FTO (A), IGF2BP3 (B), RBM15B (C), and ZC3H13 (D). (E) Substrate prediction for the m6A regulator based on the genes from Wnt signaling pathway, focal adhesion, Wnt-protein binding, and cell cycle. (F) The level of m6A modification on ACTB, CLDN11, β-catenin and WNT5B observed by IGV.
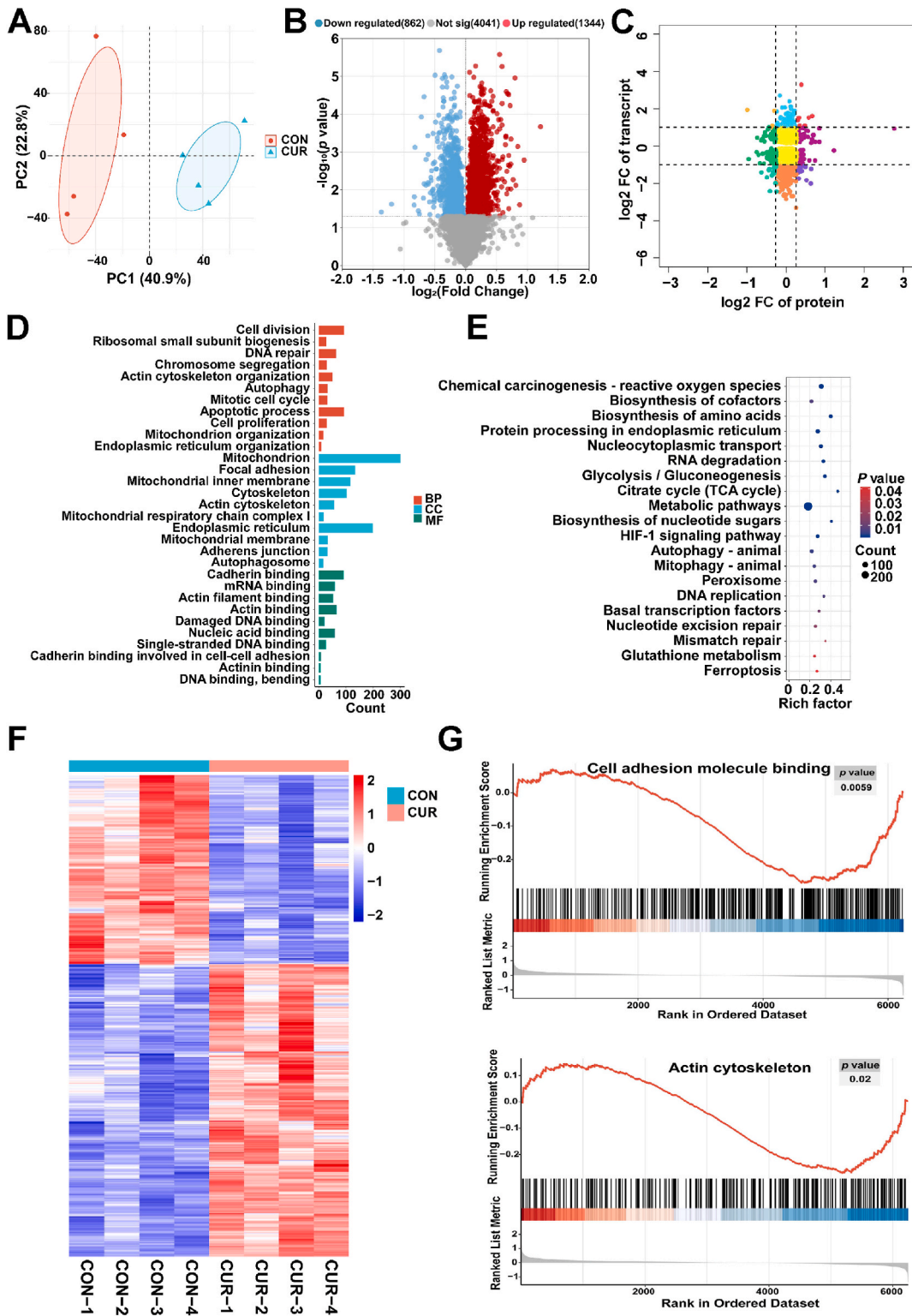
Fig. 5. (A) PCA scores plot for the protein expression in different groups. (B) The volcano plot showing the DEPs in the control and curdione-treated groups. (C) The nine-quadrant diagram depicting the correlation between protein expression and mRNA expression. (D) GO enrichment analysis of DEPs in curdione-treated and conrol groups. (E) Bubble plot of the KEGG pathway enrichment of DEPs. (F) Heatmap of parts of DEPs in curdione-treated and control groups. (G) GSEA revealed that genes in the curdione group were enriched for cell adhesion molecule binding and actin cytoskeleton.
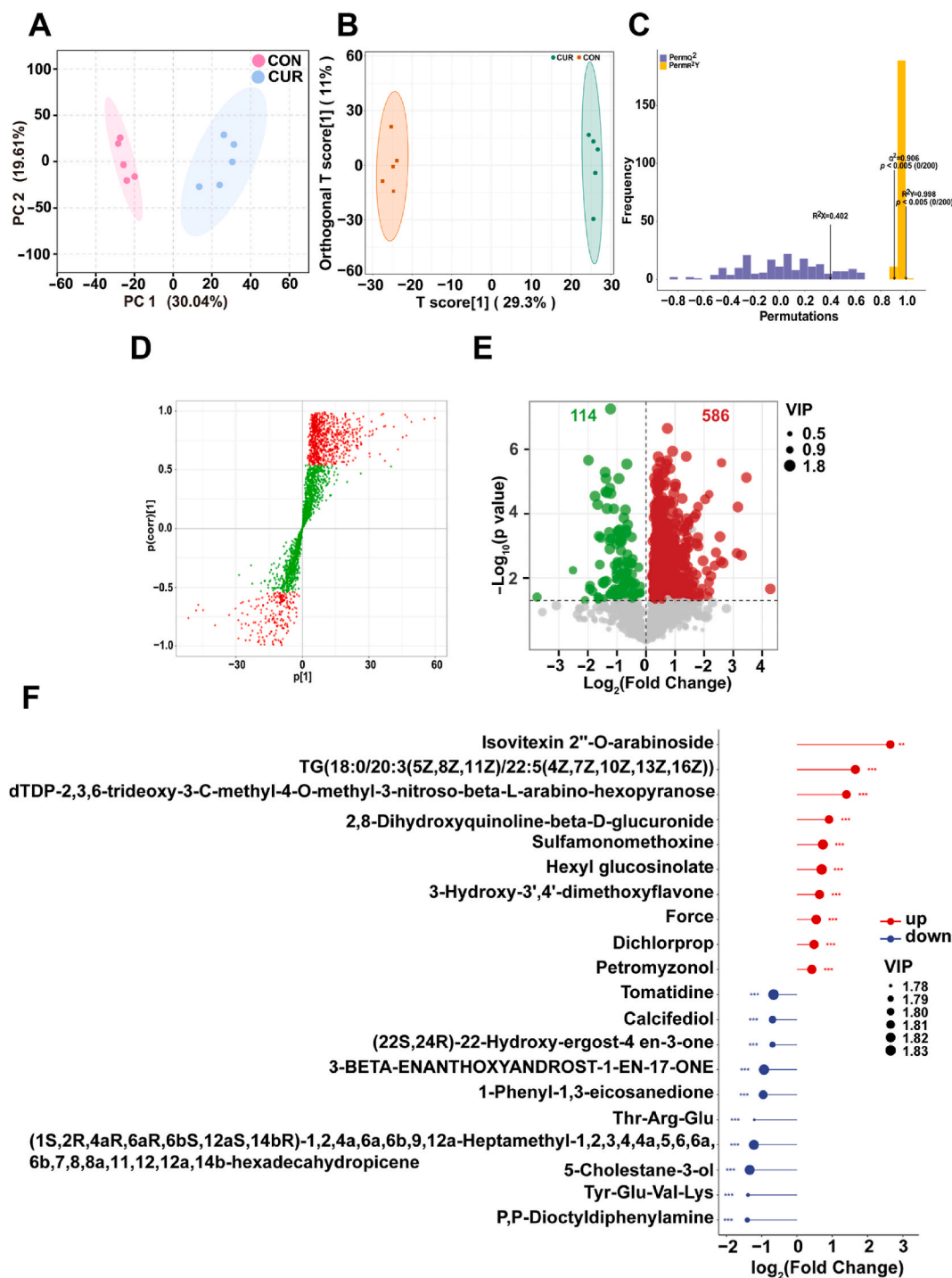
Fig. 6. (A) PCA for the content of metabolites between the control and 500 μM curdione groups. (B) OPLS-DA score plot of metabolomics data compared control and 500 μM curdione groups. (C) The permutation tests with number n = 200 for the OPLS-DA model. (D) OPLS-DA S-plots of metabonomic comparison between control and 500 μM curdione groups. The abscissa represents the covariance between principal components and metabolites, while the ordinate represents the correlation coefficient between principal components and metabolites. (E) Volcano plot of up-regulated and down-regulated metabolites in 500 μM curdione group compared with control group. (F) Top 10 metabolites of VIP among up-regulated and down-regulated DEMs.
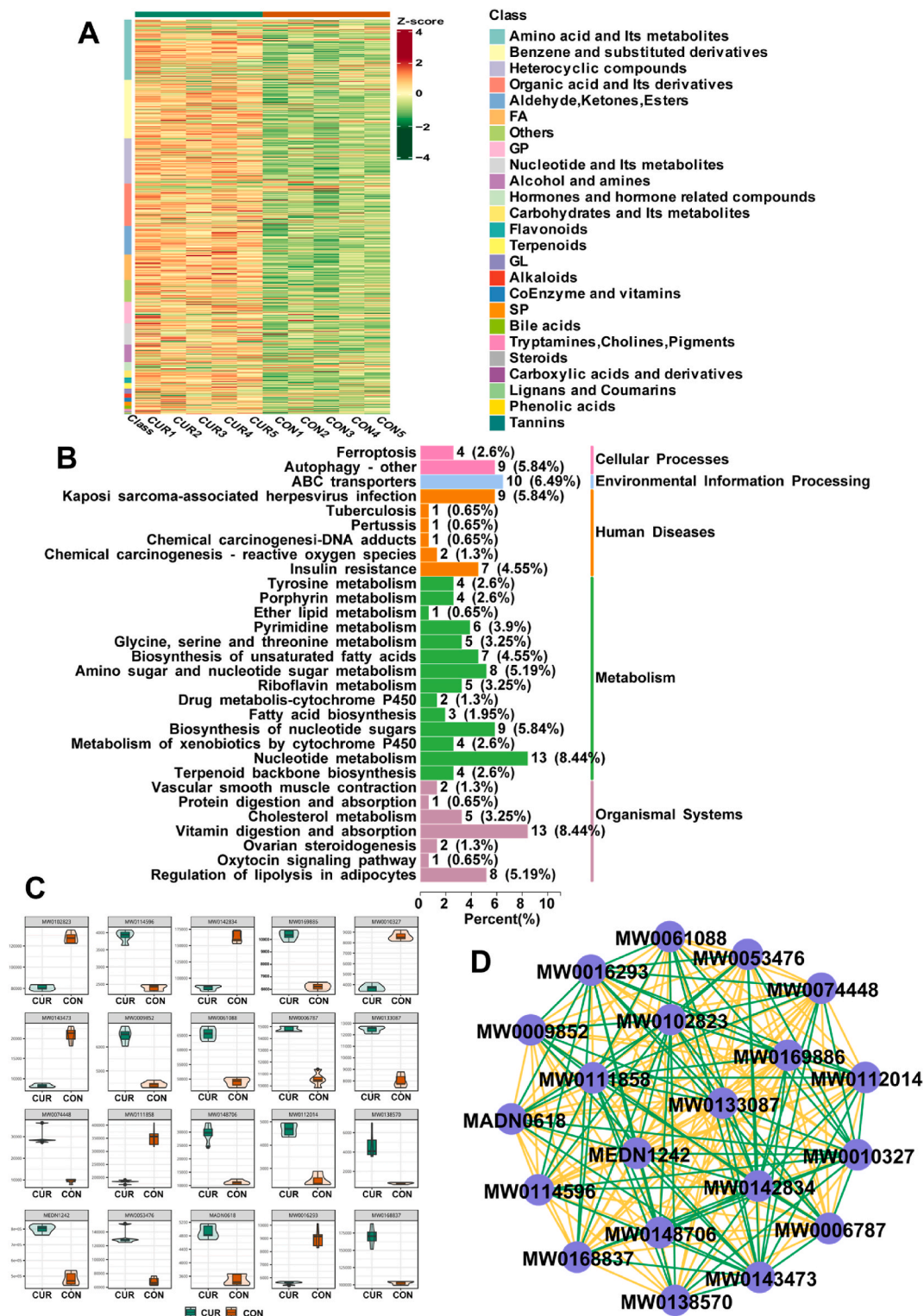
Fig. 7. (A) Cluster heatmap of DEMs. (B) After treating HTR-8/SVneo cells with curdione for 48 h, DEMs were enriched and KEGG classification map was obtained. (C) Violin plots showed the top 20 DEMs with VIP values. (D) The correlation network diagram of the top 20 DEMs of VIP value. The size of the dots is related to the degree, with larger dots indicating a greater degree. Positive correlations are indicated by yellow lines, whereas negative correlations are represented by green lines. (For interpretation of the references to colour in this figure legend, the reader is referred to the Web version of this article.)

value < 0.05, resulting in 1344 proteins with increased expression and 862 proteins with decreased expression. As depicted in Fig. 5B, red dots indicate proteins that are upregulated, whereas blue dots represent proteins that are downregulated. The correlation analysis between the overlapping genes from the m6A gene to RNA-seq genes and proteomic results was conducted using nine quadrants diagram (Fig. 5C). In total, 25 genes and proteins were discovered to show consistent changes, of which 7 showed up-regulation and 18 displayed down-regulation. The functions and regulatory mechanisms of these genes with consistent changes require further exploration.

To further analyze the signaling pathways related to the differential protein genes, proteins with $p < 0.05$ were chosen for GO (Fig. 5D) and KEGG (Fig. 5E) enrichment analysis. The results showed enrichment in KEGG pathways including mitophagy, DNA replication, glutathione metabolism, and the TCA cycle. In the biological process category in GO, proteins were mainly associated with
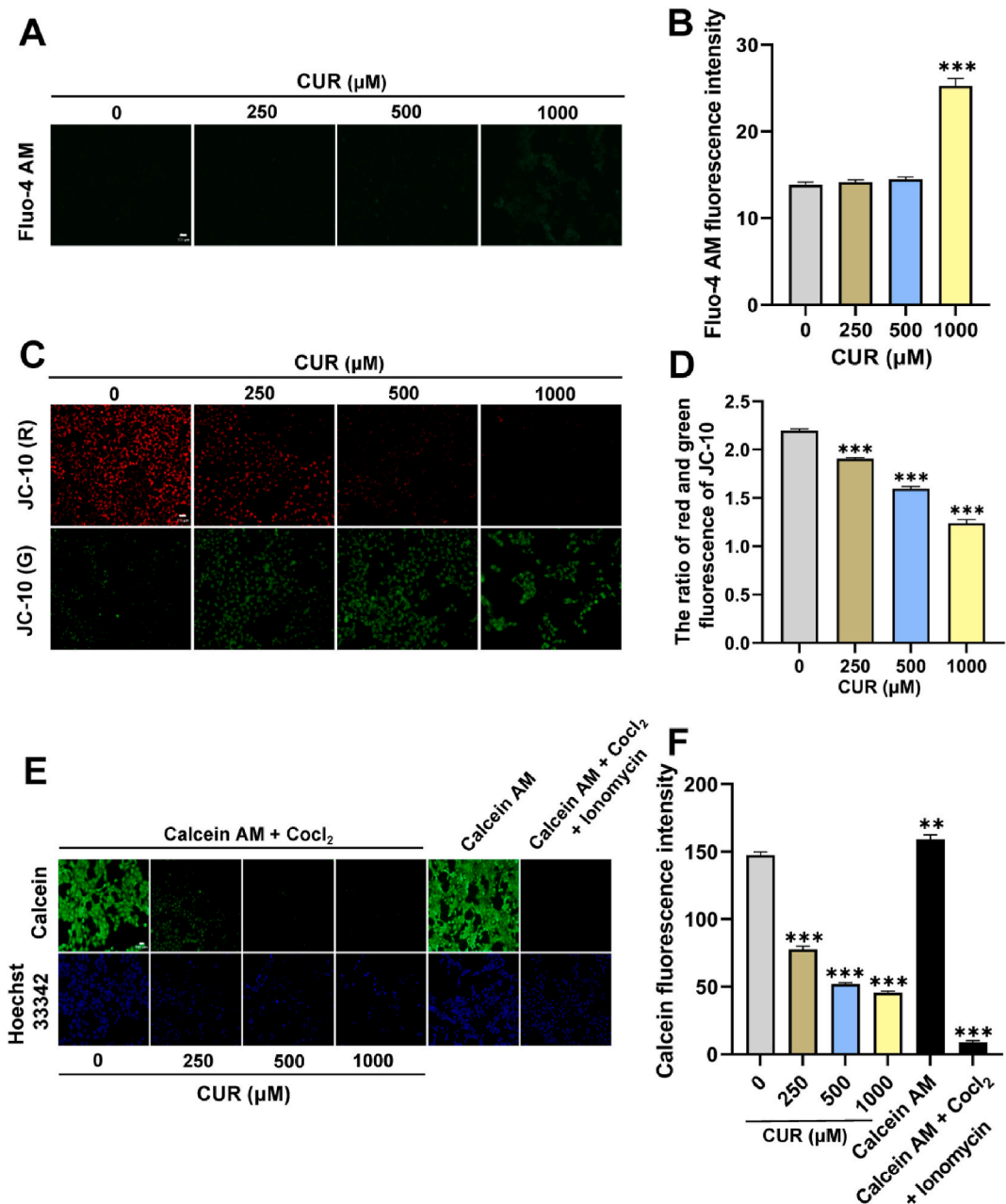

Fig. 8. Representative images (A) and quantitative results (B) of the Ca^{2+} levels was detected by Fluo-4 AM. The MMP and mPTP in curdione-treated cells were detected using JC-10 and Calcein AM probes, respectively. The fluorescent images (C) and quantitative results (D) of the JC-10 probe, as well as the fluorescent images (E) and quantitative results (F) of the Calcein AM probe in curdione-treated HTR-8/SVneo cells. **$p < 0.01$ or ***$p < 0.001$.

the apoptotic process, mitochondrion organization, mitotic cell cycle, and actin cytoskeleton organization, etc. Regarding the molecular function category, it is mainly related to cell-cell adhesion, actin binding, cadherin binding, and other processes. In addition, the enrichment of cellular components is predominantly observed in focal adhesion, cytoskeleton, adherens junction, mitochondrion, and more. The expression variations of proteins that are selected according to the criteria of p value < 0.05 and fold change >1.2 or <0.83 are depicted via a heatmap (Fig. 5F). The 493 DEPs of the heatmap are provided in Table S2.

We conducted GSEA to elucidate the signaling pathways related to curdione treatment. The results showed that the pathways of cell adhesion molecule binding and actin cytoskeleton pathways were inhibited (Fig. 5G).

3.7. Metabolomics results after curdione treatment

The results of PCA indicated distinct separation between the control group and the curdione group, suggesting significant alterations in the metabolites of HTR-8/SVneo cells treated with 500 μM curdione for 48 h (Fig. 6A). PCA efficiently extracts main information but lacks sensitivity to variables with small correlation. This limitation was addressed using orthogonal partial least squares discriminant analysis (OPLS-DA), which maximizes discrimination between groups, aiding in the identification of differential metabolites (Fig. 6B). Similarly, the OPLS-DA results indicated significant changes in metabolites between the control and 500 μM curdione groups. We considered the model to be excellent if the Q^2 value is higher than 0.9. As shown in Fig. 6C, $Q^2 = 0.906$, suggesting the model is dependable.

By utilizing the OPLS-DA model, the Variable Importance in Projection (VIP) was derived to help identify potential differentially expressed metabolites (DEMs). Metabolites with VIP values higher than 1 were generally considered to differ significantly. The OPLS-DA S-plot was used to display metabolites with VIP values above 1 (red dots) or below 1 (green dots) (Fig. 6D). The DEMs were further screened according to the criteria of VIP >1 and $p < 0.05$. The analysis revealed 700 DEMs, comprising 586 metabolites with increased expression and 114 metabolites with decreased expression (Fig. 6E). The information on 700 DEMs is listed in Table S3. Fig. 6F showed the top 10 metabolites with VIP values in the up-and down-regulated DMEs in the OPLS-DA model.

The cluster heatmap was plotted using unit variance scaling to show the abundances and classification of DEMs in the control and 500 μM curdione groups. The results showed that the dominant components of the DEMs included amino acids, benzene along with its substituted derivatives, and various heterocyclic compounds (Fig. 7A). KEGG pathway analysis was shown on DEMs, and the resulting pathways were classified. As shown in Fig. 7B, these pathways were mainly associated with metabolism, human diseases, and organismal systems. We selected the metabolism of xenobiotics by the cytochrome P450 pathway from the KEGG enrichment results
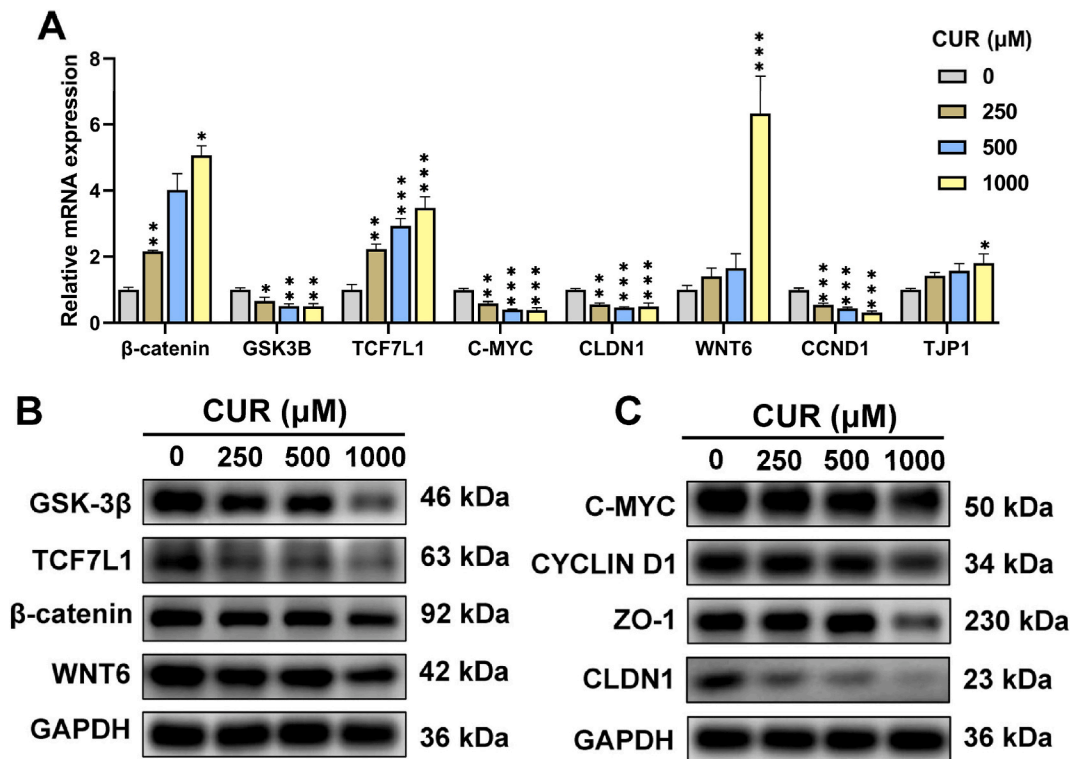

Fig. 9. (A) The mRNA level were assessed by RT-qPCR. *$p < 0.05$, **$p < 0.01$ or ***$p < 0.001$. (B) The protein expression levels of GSK-3β, TCF7L1, β-catenin, and Wnt6 in 0, 250, 500, and 1000 μM curdione treated HTR-8/SVneo cells. (C) The protein expression levels of C-MYC, CYCLIN 1, ZO-1, and CLDN1.

and identified the DEGs that regulated this pathway following curdione treatment. Through querying the genes of the above pathway using the KEGG database and combining it with the all DEGs obtained by mRNA-seq, we found that the metabolism of xenobiotics by cytochrome P450 is regulated by the DEGs *AKR1C1*. Fig. 7C displayed the top 20 DEMs for VIP values, with their full names listed in Table S4. The correlation network analysis of the top 20 DMEs with VIP values showed that the absolute value of the correlation coefficients for these metabolites was higher than 0.95, indicating a strong interaction among them (Fig. 7D).

3.8. The detrimental effects of curdione treatment on mitochondrial

As shown in Fig. 8A and B, the green fluorescence intensity was increased gradually with the treatment 0, 250, 500, and 1000 μM curdione. The results indicated that curdione increased intracellular Ca^{2+} levels and led to Ca^{2+} overload. The ratio of red and green fluorescence (Fig. 8C and D) of JC-10 decreased from 2.20 ± 0.03 in the control group to 1.24 ± 0.06 in the 1000 μM curdione group ($p < 0.05$), suggesting a decrease in the MMP of the HTR-8/SVneo cells treated with curdione. Consistently, the intensities of Calcein fluorescence were 147.62 ± 3.93, 77.82 ± 3.85, 52.02 ± 1.97, and 45.64 ± 1.85 in the 0, 250, 500, and 1000 μM curdione groups, respectively (Fig. 8E and F). Calcein's green fluorescence intensity decreased in a manner that was dependent on the dose, indicating significant induction of mPTP opening with curdione treatment.

3.9. Involved in cell cycle, tight junctions and the Wnt signaling pathway are mRNA and protein expression

Evaluation of mRNA levels was conducted using RT-qPCR to analyze the expression of genes related to cell cycle regulation, the Wnt signaling pathway, and tight junctions. Fig. 9A illustrates that curdione resulted in a decrease of *GSK3B*, *C-MYC*, and *CCND1* expression, while the level of *CLDN1*, *WNT6*, *β-catenin*, *TCF7L1*, and *TJP1* increased. As shown in Fig. 9B, western blotting analyses showed that β-catenin, TCF7L1, WNT6, and GSK-3β expression levels of were decreased following curdione treatment. The levels of C-MYC, CYCLIN D1, ZO-1, and CLDN1 (Fig. 9C) also decreased in a concentration-dependent manner in response to curdione.

4. Discussion

Omics technologies have been applied to the research of Chinese medicine and have promoted advancements in various research fields. Previous studies have revealed that the traditional Chinese medicine CangFu Daotan decoction is capable of modulating m6A modifications and suppressing the Wnt/β-catenin signaling pathway in rats with polycystic ovary syndrome, thereby regulating the expression of autophagy, apoptosis and proliferating proteins [29]. Research has found that homozygous *HNRNPC* gene knockout mice arrested gastrulation, halting development at the egg cylinder stage and subsequently being reabsorbed at different time points [30]. Alterations in *HNRNPC* gene expression level impacted embryo development. Our research revealed that the reader *HNRNPC* was involved in the Wnt signaling pathway, focal adhesion, Wnt-protein binding, and cell cycle. Additionally, proteomic results showed that curdione treatment altered protein expression levels in cells, enriching terms related to DNA replication, glutathione metabolism, mitochondrion, and the tricarboxylic acid cycle (TCA), highlighting the close association between protein expression levels and metabolic processes. Recent studies have illuminated the significant regulatory role of metabolism in embryonic development. Moreover, the results from multiple omics approaches suggested that curdione influenced cellular status by modulating gene, protein, and metabolite levels, as well as epigenetic patterns.

The findings of this study revealed that exposure to curdione resulted in the accumulation of ROS and elevated Ca^{2+} levels. ROS, produced during oxidation-reduction processes, play a vital role in the cytotoxic effects induced by curdione. Excessive Ca^{2+} levels are implicated in ROS generation, leading to aggravated mitochondrial damage [31]. Increased levels of Ca^{2+} can have an adverse impact on the functioning of mitochondria, causing the mPTP to open and resulting in the liberation of cytochrome *c* and GSH-antioxidative enzymes [32]. Accumulation of ROS is recognized to induce MMP collapse and the opening of the mPTP [33]. Elevated Ca^{2+} levels during curdione treatment trigger the opening of mPTP, subsequently worsening mitochondrial dysfunction [34]. In this study, we have shown that curdione can induce mitochondrial toxicity by causing Ca^{2+} overload and excessive generation of ROS. In short, curdione induces the occurrence of oxidative stress and calcium overload in HTR-8/SVneo cells, and affects mitochondrial function.

It has been hypothesized that oxidative stress may also activate the Wnt/β-Catenin signaling pathway [35]. The Wnt/β-catenin signaling pathway has been conserved throughout evolution and plays an essential role in regulating numerous reproductive and physiological processes, particularly in the embryonic development, including the differentiation and proliferation of the trophoblast [36,37]. The Wnt signaling pathway serves as a fundamental signal transduction pathway that is critical for both human development and the maintenance of stem cell properties. A study revealed that compared with the WT groups, the low-density lipoprotein receptor-related protein 5 knockout mouse group showed down-regulation of claudin-5, as well as down-regulation of Wnt5a, Wnt7b, and Wnt10b, resulting in impaired retinal angiogenesis [38]. ZO-1 knockout in mice caused the attenuation of the Wnt-β-catenin signaling, which led to augmented sensitivity to mucosal insults and compromised tissue repair [39]. The results of our study demonstrate a significant down-regulation of Wnt6, β-catenin, claudin-1, and ZO-1 following curdione treatment, suggesting the disruption of tight junctions in HTR-8/SVneo cells. Wnt6 expression is significantly up-regulated at the mRNA level, possibly as a result of post-transcriptional regulation. However, this study does not extensively explore the analysis of transcriptomics, proteomics, and metabolomics associations, and further validation of dysregulated genes was not conducted through overexpression or knockdown methods.

5. Conclusion

In conclusion, the current study has analyzed the effect of curdione on HTR-8/SVneo cells. The results show that curdione exposure induces ROS accumulation, mitochondrial dysfunction, DNA damage and disruption of tight junctions in HTR-8/SVneo cells. Our research findings indicate that the reproductive toxicity mediated by curdione may be associated with its induction of mitochondrial dysfunction, DNA damage, and disruption of tight junctions. Based on these results, we theorize that the underlying mechanisms of curdione-induced toxicity damage potentially involve the Wnt signaling pathway.

Data availability statement

Data associated with study have deposited into a publicly available repository. MeRIP data have been deposited at [datatype-specific repository (https://www.ncbi.nlm.nih.gov/geo/) with accession numbers GSE269246.

Funding

CRediT authorship contribution statement

Qibin Wu: Writing – original draft, Investigation, Funding acquisition, Formal analysis, Conceptualization. **Mengting Chen:** Writing – original draft, Investigation, Formal analysis. **Yifan Lin:** Writing – original draft, Investigation, Formal analysis. **Jian Zhang:** Writing – original draft, Investigation. **Xinyue Gao:** Writing – original draft, Investigation. **Yajiao Wu:** Writing – original draft, Investigation. **Caijin Wu:** Writing – original draft, Investigation. **Jiaxin Wen:** Data curation. **Jiaqi Li:** Data curation. **Chutao Li:** Data curation. **Wenqiang Bao:** Data curation. **Dongcheng Zhang:** Data curation. **Meijin Zheng:** Writing – review & editing. **An Zhu:** Writing – review & editing, Funding acquisition, Conceptualization.

Declaration of competing interest

The authors declare that they have no known competing financial interests or personal relationships that could have appeared to influence the work reported in this paper.

Abbreviations

DEPs	differentially expressed proteins
DEG	differentially expressed gene
DEMs	differentially expressed metabolites
DMSO	dimethyl sulfoxide
GO	Gene Ontology
GSEA	gene set enrichment analysis
HPLC	high-performance liquid chromatography
IGF2BP3	IGF2BP3 insulin like growth factor 2 mRNA binding protein 3
KEGG	Kyoto Encyclopedia of Genes and Genomes
ROS	reactive oxygen species
MMP	mitochondrial membrane potential

Appendix A. Supplementary data

Supplementary data to this article can be found online at https://doi.org/10.1016/j.heliyon.2024.e38650.

References

[1] H. Fang, B. Gao, Y. Zhao, X. Fang, M. Bian, Q. Xia, Curdione inhibits thrombin-induced platelet aggregation via regulating the AMP-activated protein kinase-vinculin/talin-integrin αIIbβ3 sign pathway, Phytomedicine 61 (2019) 152859.
[2] D. Zhang, W. Qiao, Y. Zhao, H. Fang, D. Xu, Q. Xia, Curdione attenuates thrombin-induced human platelet activation: β1-tubulin as a potential therapeutic target, Fitoterapia 116 (2017) 106–115.
[3] C.C. Wang, L. Li, L.Y. Tang, P.C. Leung, Safety evaluation of commonly used Chinese herbal medicines during pregnancy in mice, Hum. Reprod. 27 (2012) 2448–2456.

[4] X. Meng, T. Zhang, Y. Li, Q. Pan, J. Jiang, Y. Luo, L. Chong, Y. Yang, S. Xu, L. Zhou, Z. Sun, The toxicokinetic profile of curdione in pregnant SD rats and its transference in a placental barrier system detected by LC-MS/MS, Regul. Toxicol. Pharmacol. 71 (2015) 158–163.

[5] S.K. Yan, R.H. Liu, H.Z. Jin, X.R. Liu, J. Ye, L. Shan, W.D. Zhang, "Omics" in pharmaceutical research: overview, applications, challenges, and future perspectives, Chin. J. Nat. Med. 13 (2015) 3–21.

[6] J. Ma, B. Song, Z. Wei, D. Huang, Y. Zhang, J. Su, J.P. de Magalhães, D.J. Rigden, J. Meng, K. Chen, m5C-Atlas: a comprehensive database for decoding and annotating the 5-methylcytosine (m5C) epitranscriptome, Nucleic Acids Res. 50 (2022) D196–d203.

[7] B. Song, Y. Tang, K. Chen, Z. Wei, R. Rong, Z. Lu, J. Su, J.P. de Magalhães, D.J. Rigden, J. Meng, m7GHub: deciphering the location, regulation and pathogenesis of internal mRNA N7-methylguanosine (m7G) sites in human, Bioinformatics 36 (2020) 3528–3536.

[8] M. Chen, C.M. Wong, The emerging roles of N6-methyladenosine (m6A) deregulation in liver carcinogenesis, Mol. Cancer 19 (2020) 44.

[9] K. Chen, Z. Wei, Q. Zhang, X. Wu, R. Rong, Z. Lu, J. Su, J.P. de Magalhães, D.J. Rigden, J. Meng, WHISTLE: a high-accuracy map of the human N6-methyladenosine (m6A) epitranscriptome predicted using a machine learning approach, Nucleic Acids Res. 47 (2019) e41–e.

[10] Y. Zhang, J. Jiang, J. Ma, Z. Wei, Y. Wang, B. Song, J. Meng, G. Jia, J.P. de Magalhães, D.J. Rigden, D. Hang, K. Chen, DirectRMDB: a database of post-transcriptional RNA modifications unveiled from direct RNA sequencing technology, Nucleic Acids Res. 51 (2023) D106–D116.

[11] B. Song, D. Huang, Y. Zhang, Z. Wei, J. Su, J. Pedro de Magalhães, D.J. Rigden, J. Meng, K. Chen, m6A-TSHub: unveiling the context-specific m6A methylation and m6A-affecting mutations in 23 human tissues, Dev. Reprod. Biol. 21 (2023) 678–694.

[12] G. Zheng, J.A. Dahl, Y. Niu, P. Fedorcsak, C.M. Huang, C.J. Li, C.B. Vågbø, Y. Shi, W.L. Wang, S.H. Song, Z. Lu, R.P. Bosmans, Q. Dai, Y.J. Hao, X. Yang, W.M. Zhao, W.M. Tong, X.J. Wang, F. Bogdan, K. Furu, C. He, ALKBH5 is a mammalian RNA demethylase that impacts RNA metabolism and mouse fertility, Mol. Cell 49 (2013) 18–29.

[13] F. Wang, Z. Sun, Q. Zhang, H. Yang, G. Yang, Q. Yang, Y. Zhu, W. Wu, W. Xu, X. Wu, Curdione induces ferroptosis mediated by m6A methylation via METTL14 and YTHDF2 in colorectal cancer, Chin. Med. 18 (2023) 122.

[14] J.K. Nicholson, J.R. Everett, J.C. Lindon, Longitudinal pharmacometabonomics for predicting patient responses to therapy: drug metabolism, toxicity and efficacy, Expet Opin. Drug Metabol. Toxicol. 8 (2012) 135–139.

[15] J. Li, W.H. Bian, J. Wan, J. Zhou, Y. Lin, J.R. Wang, Z.X. Wang, Q. Shen, K.M. Wang, Curdione inhibits proliferation of MCF-7 cells by inducing apoptosis, Asian Pac. J. Cancer Prev. 15 (2014) 9997–10001.

[16] N. Krishnamurthy, R. Kurzrock, Targeting the Wnt/beta-catenin pathway in cancer: update on effectors and inhibitors, Cancer Treat Rev., 62 (2018) 50–60.

[17] X. Lin, J. Zhang, Z. Wu, Y. Shi, M. Chen, M. Li, H. Hu, K. Tian, X. Lv, C. Li, Y. Liu, X. Gao, Q. Yang, K. Chen, A. Zhu, Involvement of autophagy in mesaconitine-induced neurotoxicity in HT22 cells revealed through integrated transcriptomic, proteomic, and m6A epitranscriptomic profiling, Front. Pharmacol. 15 (2024) 1393717.

[18] Z. Liang, H. Ye, J. Ma, Z. Wei, Y. Wang, Y. Zhang, D. Huang, B. Song, J. Meng, D.J. Rigden, K. Chen, m6A-Atlas v2.0: updated resources for unraveling the N6-methyladenosine (m6A) epitranscriptome among multiple species, Nucleic Acids Res. 52 (2024) D194–d202.

[19] T.L. Bailey, STREME: accurate and versatile sequence motif discovery, Bioinformatics 37 (2021) 2834–2840.

[20] D. Kim, J.M. Paggi, C. Park, C. Bennett, S.L. Salzberg, Graph-based genome alignment and genotyping with HISAT2 and HISAT-genotype, Nat. Biotechnol. 37 (2019) 907–915.

[21] H. Varet, L. Brillet-Guéguen, J.Y. Coppée, M.A. Dillies, SARTools: a DESeq2- and EdgeR-based R pipeline for comprehensive differential analysis of RNA-seq data, PLoS One 11 (2016) e0157022.

[22] B. Song, X. Wang, Z. Liang, J. Ma, D. Huang, Y. Wang, J.P. de Magalhães, D.J. Rigden, J. Meng, G. Liu, K. Chen, Z. Wei, RMDisease V2.0: an updated database of genetic variants that affect RNA modifications with disease and trait implication, Nucleic Acids Res. 51 (2023) D1388–D1396.

[23] B. Song, K. Chen, Y. Tang, Z. Wei, J. Su, J.P. de Magalhães, D.J. Rigden, J. Meng, ConsRM: collection and large-scale prediction of the evolutionarily conserved RNA methylation sites, with implications for the functional epitranscriptome, Briefings Bioinf. 22 (6) (2021) bbab088.

[24] Y. Wang, K. Chen, Z. Wei, F. Coenen, J. Su, J. Meng, MetaTX: deciphering the distribution of mRNA-related features in the presence of isoform ambiguity, with applications in epitranscriptome analysis, Bioinformatics, 37 (2021) 1285–1291.

[25] G. Dennis Jr., B.T. Sherman, D.A. Hosack, J. Yang, W. Gao, H.C. Lane, R.A. Lempicki, DAVID: database for annotation, visualization, and integrated discovery, Genome Biol. 4 (2003) P3.

[26] Y. Wu, X. Chen, W. Bao, X. Hong, C. Li, J. Lu, D. Zhang, A. Zhu, Effect of humantenine on mRNA m6A modification and expression in human colon cancer cell line HCT116, Genes 13 (5) (2022) 781.

[27] Y. Wu, W. Bao, J. Ren, C. Li, M. Chen, D. Zhang, A. Zhu, Integrated profiles of transcriptome and mRNA m6A modification reveal the intestinal cytotoxicity of aflatoxin B1 on HCT116 cells, Genes 14 (1) (2022) 79.

[28] X. Shen, M. Chen, J. Zhang, Y. Lin, X. Gao, J. Tu, K. Chen, A. Zhu, S. Xu, Unveiling the impact of ApoF deficiency on liver and lipid metabolism: insights from transcriptome-wide m6A methylome analysis in mice, Genes 15 (3) (2024) 347.

[29] Y. Zhang, H. Zhou, C. Ding, The ameliorative effect of CangFu Daotan decoction on polycystic ovary syndrome of rodent model is associated with m6A methylation and Wnt/β-catenin pathway, Gynecol Endocrinol. 39 (1) (2023) 2181637.

[30] D.J. Williamson, S. Banik-Maiti, J. DeGregori, H.E. Ruley, hnRNP C is required for postimplantation mouse development but is dispensable for cell viability, Mol. Cell Biol. 20 (2000) 4094–4105.

[31] S. Kovac, A.M. Domijan, M.C. Walker, A.Y. Abramov, Seizure activity results in calcium- and mitochondria-independent ROS production via NADPH and xanthine oxidase activation, Cell Death Dis. 5 (2014) e1442.

[32] T.I. Peng, M.J. Jou, Oxidative stress caused by mitochondrial calcium overload, Ann. N. Y. Acad. Sci. 1201 (2010) 183–188.

[33] C.C. Wang, K.M. Fang, C.S. Yang, S.F. Tzeng, Reactive oxygen species-induced cell death of rat primary astrocytes through mitochondria-mediated mechanism, J. Cell. Biochem. 107 (2009) 933–943.

[34] J. Zhan, X. Li, D. Luo, W. Yan, Y. Hou, Y. Hou, S. Chen, J. Luan, Q. Zhang, D. Lin, Polydatin attenuates OGD/R-Induced neuronal injury and spinal cord ischemia/reperfusion injury by protecting mitochondrial function via Nrf2/ARE signaling pathway, Oxid. Med. Cell. Longev. 2021 (2021) 6687212.

[35] A. Andersson-Sjöland, J.C. Karlsson, K. Rydell-Törmänen, ROS-induced endothelial stress contributes to pulmonary fibrosis through pericytes and Wnt signaling, Lab Invest. 96 (2016) 206–217.

[36] T. Sidrat, Z.U. Rehman, M.D. Joo, K.L. Lee, I.K. Kong, Wnt/β-catenin pathway-mediated PPARδ expression during embryonic development differentiation and disease, Int. J. Mol. Sci. 22 (4) (2021) 1854.

[37] N. Li, D.M. Sun, Y.Z. Chang, X.N. Li, J.L. Li, T.Q. Wang, Di-(2-ethylhexyl) phthalate exacerbates abnormalities of testicular development in F1 males via inhibition the Wnt/β-catenin signaling pathway, Environ Pollut. 343 (2024) 123170.

[38] J. Chen, A. Stahl, N.M. Krah, M.R. Seaward, J.S. Joyal, A.M. Juan, C.J. Hatton, C.M. Aderman, R.J. Dennison, K.L. Willett, P. Sapieha, L.E. Smith, Retinal expression of Wnt-pathway mediated genes in low-density lipoprotein receptor-related protein 5 (Lrp5) knockout mice, PLoS One 7 (2012) e30203.

[39] W.T. Kuo, L. Zuo, M.A. Odenwald, S. Madha, G. Singh, C.B. Gurniak, C. Abraham, J.R. Turner, The tight junction protein ZO-1 is dispensable for barrier function but critical for effective mucosal repair, Gastroenterology 161 (2021) 1924–1939.